UC Santa Barbara
UC Santa Barbara Previously Published Works

Title

Effects of Tow-Scale Holes on the Mechanical Performance of a 3D Woven C/SiC Composite

Permalink

Journal

ISSN

Authors

Shaw, John H
Rossol, Michael N
Marshall, David B
et al.

Publication Date

DOI

journal

Effects of Tow-Scale Holes on the Mechanical Performance of a 3D Woven C/SiC Composite

John H. Shaw,[‡] Michael N. Rossol,[‡] David B. Marshall,[§] and Frank W. Zok[‡,†]

[‡]Materials Department, University of California, Santa Barbara, California 93106

[§]Teledyne Scientific Company, Thousand Oaks, California 91360

This article addresses the effects of small holes (1–2 mm in diameter) on the tensile properties of a woven C/SiC composite. Holes are introduced by one of two methods: by insertion of fugitive rods into the woven preform before adding the matrix or by drilling after panel fabrication. The tensile strength exhibits only a weak sensitivity to the presence of holes, regardless of the manner in which the holes are introduced. Nevertheless, woven holes appear to be somewhat less detrimental to strength. The effects are attributed to the fact that the tows in specimens with woven holes are locally intact and thus contribute to load-bearing. Full-field strain maps reveal strong spatial periodicity, reflecting the underlying crack pattern and weave geometry. Even when averaged over lengths equal to the unit cell dimensions, the strains exhibit periodicity, with a wavelength dictated by the unit cell dimensions. When holes are present, the strain patterns reflect a convolution of the effects of weave geometry and strain concentrations near the holes. The results have implications for development of high-fidelity models for these composites: notably, in selection of a suitable representative volume element and for modeling schemes that capture the stochastic nature of cracking.

I. Introduction

TEXTILE-BASED ceramic matrix composites (CMCs) offer a unique combination of low density, high-temperature performance, and damage tolerance. These features make CMCs attractive for use in hot components in propulsion systems of gas turbine and scramjet engines. In some applications, it is envisioned that the components will contain geometric (stress-concentrating) features such as holes, for cooling, fuel passage, or attachment. For this reason, a great deal of study has been undertaken previously to characterize the notch sensitivity of strength of a wide range of CMCs, including C/C, C/CAS, oxide/oxide, and SiC/SiC systems.[1–7]

Despite popular notions of "notch-insensitivity," even the toughest CMCs exhibit some dependence of ultimate tensile strength (UTS) and other performance metrics on notches or holes. The degree of sensitivity depends on: (i) the intrinsic properties of the composite, notably its (generally anisotropic) elastic, plastic, and fracture characteristics; and (ii) the notch size and shape, characterized by the principal radii a and b (for elliptical holes) and the ratios a/b and a/w (w being the half specimen width).[4] The UTS generally decreases with increasing a (for fixed a/b and a/w) and increasing a/w (for fixed a and a/b). Such effects have been found in most

composite systems for specimens with circular holes of size $a \geq 1$ mm.[1–4] Where attempts have been made to compute the stress and strain distributions ahead of holes at the onset of fracture (using an appropriate elastic/plastic constitutive law), the local conditions appear to be consistent with a point stress failure criterion. That is, fracture occurs when the local tensile stress exceeds a critical value (notably the unnotched UTS) at a characteristic distance from the hole, typically about 1 mm. While perhaps fortuitous, the characteristic dimension appears to coincide approximately with the in-plane dimensions of the constituent tows. In systems that exhibit oxidative degradation, notch sensitivity can also be manifested in a reduced lifetime under static loading conditions.[8,9]

In most cases, holes are introduced into composite components or specimens by conventional machining methods after processing has been completed. Alternatively, they can be introduced into the woven preform without cutting fibers prior to densification. This method has been used successfully in fiber-reinforced polymer matrix composites (PMCs)[10,11] and in ceramic composites.[12] One way of achieving this goal is to insert fugitive rods of prescribed diameter into the fiber preform at the intended locations of holes, and then introduce the matrix with the rods in place. The rods can be inserted either (i) after weaving, by deflecting fiber tows around the rod (without causing significant damage to the fibers), provided the rod diameter is comparable to the fiber tow size, or (ii) during weaving, using a modified local weave structure around the rod for larger holes.[12] The end result is a composite with continuous, unbroken fibers around the holes. When introduced in this manner in PMCs, the holes have been found to have a smaller effect on the knockdown in tensile strength relative to that when holes are machined after processing has been completed.[10,11] In CMCs, there is an additional benefit of avoiding exposure of cut fibers to the service environment. These benefits are especially important in applications where rows of closely spaced holes are needed, as in many turbine combustors and blades.

This study is part of a broader initiative on high-temperature CMCs intended for use in propulsion systems in hypersonic flight vehicles.[13] Specifically, in this study, we investigate the effects of small holes on the tensile properties of a woven, anisotropic C/SiC CMC. The holes are introduced by the two methods described above: notably, by insertion of rods into the woven preform before adding the matrix and by conventional machining after fabrication. The effects of rod insertion on local tow distortions are probed through analysis of high-resolution optical scans of the partially processed composite. Following this, tensile tests are performed using digital image correlation (DIC) to characterize the surface displacement and strain fields around the holes. The effects of competing size scales—notably, those of the hole and the unit cell of the weave—are addressed.

II. Material System and Weave Characterization

(1) Material Structure and Fabrication

The material of interest in this study is a C/SiC composite formed from a woven preform of T300-6K carbon fibers with a three-layer angle-interlock architecture. The weft tows, which are relatively straight, are in three layers locked together by the warp tows, which follow approximately sinusoidal paths passing through the thickness of the composite (Fig. 1). The weft tows situated in one of the two outer layers are designated as "surface wefts" and those in the center as "center wefts". The preform is similar to that used in previous studies[14–16] with the exception of the warp tow wavelength. The unit cell dimensions in the present material are 7.5 mm in the warp direction and 5.1 mm in the weft direction. The fiber volume fractions were calculated from the manufacturer's data on fiber tow yield, the measured specimen thickness and the unit cell dimensions; they are $f_{warp} = 11\%$ and $f_{weft} = 22\%$, in the warp and the weft directions, respectively.

Coatings of pyrolytic carbon and then SiC were infiltrated into the fiber preform by chemical vapor infiltration (CVI). The thickness of the pyrolytic carbon coating was relatively uniform (~1 μm) on all the fibers, whereas the SiC coating thickness varied with the location of the fibers (Fig. 1). Near the centers of the tows, the individual fiber coatings of SiC were very thin or nonexistent (0–0.01 μm thickness), whereas near the perimeter most of the space between fibers was filled with SiC. The perimeter of each tow was surrounded by a continuous layer of SiC of thickness ~30–50 μm. This layer was sufficiently thick to bond all of the fiber tows together and form a rigid composite. The layer occupies about 20% of the volume between fiber tows.

Matrix material was then introduced into the remaining inter-tow regions by repeated cycles of infiltration and pyrolysis of slurries of SiC particles in preceramic polymer (AHPCS polymer, Starfire Systems Inc., Schenectady, NY). Images of the panel surface after CVI processing and cross sections of the fully processed material are shown in Fig. 1. One notable feature, evident in the higher magnification images, is the presence of cracks in the matrix at locations adjacent to transverse tows [indicated with arrows in Figs. 1(b) and (f)]. These are attributed to thermal expansion mismatch between the fibers and the matrix along with the temperature change following pyrolysis of the precursor. Some of these cracks are clearly open whereas others appear to have been filled during the PIP process. Some of the PIP material had also penetrated into the fiber tows [Fig. 2(c)], presumably via the cracks in the CVI SiC overlayer.

Small holes were introduced into the panel in two ways. In the first, holes were machined into specimens using a 1 mm diameter diamond jeweler's drill in a CNC mill. The mill had been programmed to make 5 μm advances with intervening coolant flushes to minimize damage. The resulting holes were 1.0–1.2 mm in diameter.

In the second, holes were created within the woven preform *prior to CVI*. This was accomplished by gently inserting graphite rods, with smoothly pointed ends and diameter 2 mm, through the woven preform at select locations. Through this operation the tows surrounding the rod were displaced laterally by a small amount with minimal fiber damage. The rods were removed after the pyrolytic carbon coating step, leaving behind approximately circular holes within the partially densified preform [Fig. 3(a)]. After adding the CVI SiC coating, the preform was characterized using procedures outlined below, prior to PIP processing. The resulting holes were 1.6–2.0 mm in diameter.

(2) Characterization of Weave Structure

The effects of inserting the rods into the preform on the surrounding tow locations were characterized by measuring the deviations of the warp crown locations from their ideal positions in a perfect panel.[17] The locations of the warp crowns were identified from high-resolution (1200 dpi) scanned optical images of the partially densified panel (after the CVI SiC processing step mentioned above) using a computational feature-finding algorithm and analyzed following a procedure developed previously.[17]

The features of interest—in this case the warp crowns—were identified in the following way. First, a set of *n* representative images of warp crowns were selected randomly from the entire image. Next, using a template matching algorithm, potential matches for each of the *n* images (or templates) with features on the image were identified. For each successful match, the template location (once aligned
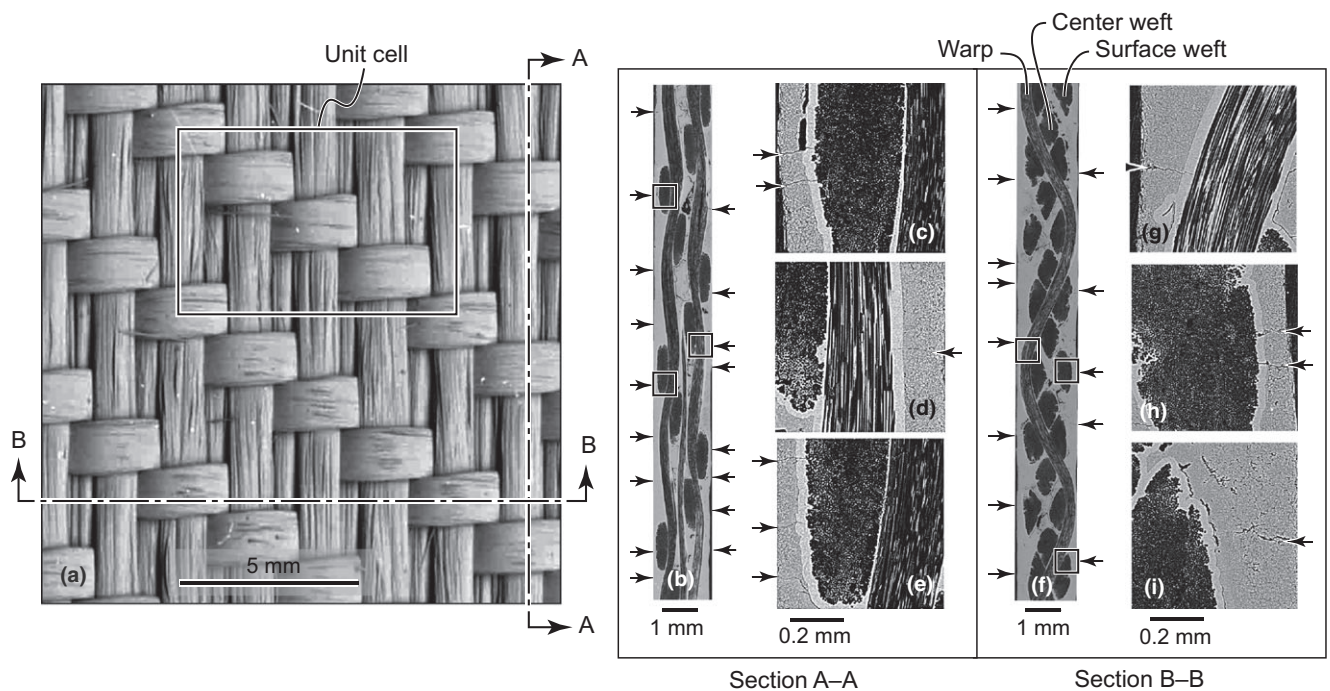

Fig. 1. (a) Plan view of the partially densified composite. (b), (f) Sections of the fully densified material along the weft and warp orientations, respectively. Preexisting matrix cracks are indicated by arrows. (c)–(e), (g)–(i) Higher magnification images of matrix cracks, outlined in (b) and (f).
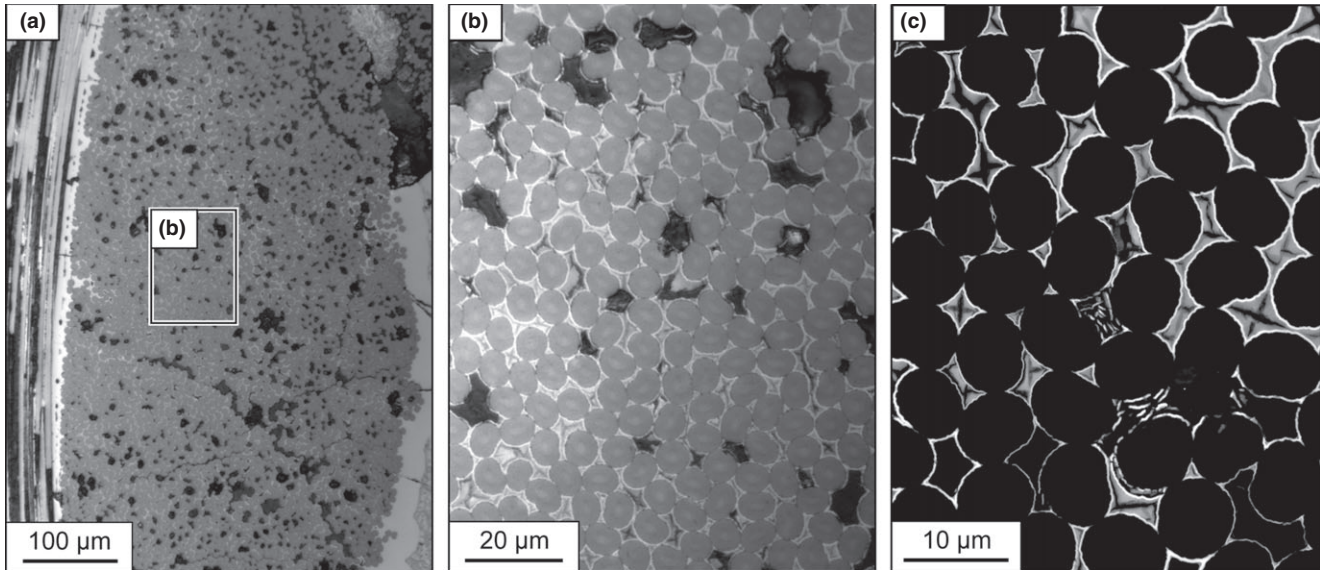
Fig. 2. Higher magnification (a), (b) optical and (c) SEM views of the tow interior in the fully processed state.
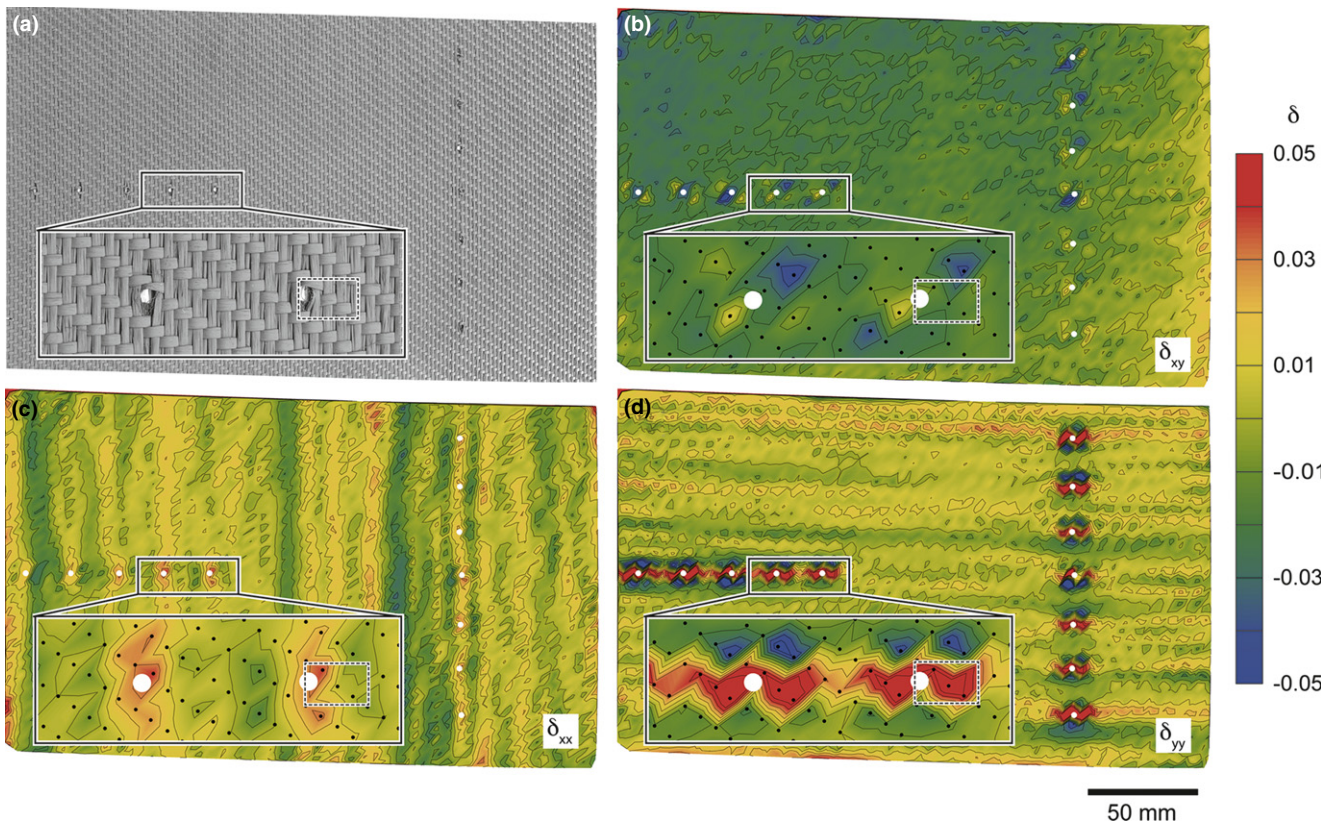

Fig. 3. (a) Plan view of the panel with woven holes. (b,c,d) Spatial variations of computed δ_{xy}, δ_{xx}, and δ_{yy}. Dashed rectangles in the insets represent one unit cell of the weave.

with the feature) was used as an estimate of the warp crown location. Positive matches were grouped spatially and the average position of each group was computed. In addition, the match probability (i.e., the fractional number of templates that had been matched to each warp crown) was also computed. Features with a match probability of <10% were deemed to be false positives and were therefore excluded from further analysis. Following this procedure, about 99% of warp crowns were correctly identified; the remaining crowns and their locations were identified manually. Segments of incomplete tows at the panel edges were excluded from the analysis, thereby yielding a rectangular data array.

Once identified, the warp crown locations were used as fiducial markers of the underlying tow locations. The coordinates (x_i, y_i) of each crown were compared with the expected coordinates $(\bar{x}_i, \bar{y}_i)$ in an ideal orthogonal weave to calculate the local deviation (u_i, v_i), defined by the following equation:

$$(u_i, v_i) = (x_i, y_i) - (\bar{x}_i, \bar{y}_i) \qquad (1)$$

The parameters characterizing the unit cell of the ideal weave were computed from a corresponding set of measurements on a separate (hole-free) panel made in the same weaving run, as detailed elsewhere.[17] The cell dimensions of

the latter panel were taken as the average separation distances between nodes in the x- and y-directions and taking the ideal angle between warp and weft tows to be 90°. Once such cell is illustrated in Fig. 1.

Local variations in the tow positions were amplified using spatial differentiation as a filter.[17] The spatial derivatives were calculated at each nodal location within the data array from the slopes of linear fits to the deviation fields, $u(x,y)$ and $v(x,y)$, over an area equivalent to one unit cell of the weave structure centered on each nodal location [Fig. 1(a)]. The spatial derivatives $\delta_{xx} = \partial u/\partial x$ and $\delta_{yy} = \partial v/\partial y$ give direct measures of the local variations in packing density[‡] of weft tows and warp tows, respectively. The other derivative, $\delta_{xy} = (\partial u/\partial y + \partial v/\partial x)/2$, is a measure of the rotation of the two tow populations with respect to each other[§] relative to that in a perfect orthogonal weave.[17] Maps of these spatial derivatives are shown in Fig. 3. Measurements of average values and standard deviations of these derivatives for two composite panels—one with an array of holes introduced using graphite rods and the other without holes (from an earlier study[17])—are summarized in Fig. 4.

The variations in δ_{xy} in the present panel are predominantly *long-range* in nature; a nearly uniform gradient is evident across the panel diagonal from the top left to the bottom right in Fig. 3(b). As discussed in Rossol *et al.*,[17] the nonzero values of δ_{xy} are attributable to shear of the panel from handling after weaving, which causes the angle between warp and weft tows to deviate from 90°. Its average value ($\delta_{xy} = -0.014$) corresponds to an angle of 88.4° between the warp and the weft tows, whereas its standard deviation corresponds to a range from 87° to 90°. These values are only slightly larger in this panel than those in the panel without holes. [It is evident from Fig.3(b) that local deformation of the preform due to the presence of the holes does not contribute significantly to the mean and standard deviation of δ_{xy} because the disturbance to the δ_{xy} field due to the holes is small in magnitude and localized to a very small area surrounding each hole.)

The spatial variations in δ_{xx} and δ_{yy} are characterized predominantly by periodic *short-range* fluctuations over length scales of a few multiples of the unit cell dimensions. These fluctuations are manifested in the form of bands of either dilation (positive δ) or compaction (negative δ). In addition, very near the holes, δ_{yy} (≈ 0.05) is about an order of magnitude greater than average; the effect persists over an apparent distance of about one unit cell away from the holes [see inset on Fig. 3(d)]. [As the strains are computed over distances equal to the unit cell dimensions, the apparent strain within an individual cell can be the result of a large displacement of *a single warp crown* adjacent to the hole. Indeed, this appears to be the case for many of the holes in Fig. 3(a)]. In contrast, the local values of δ_{xy} and δ_{xx} are elevated only very slightly relative to their respective averages [insets in Figs. 3(b) and (c)].

The fact the local deviation of the warp packing density (δ_{yy}) adjacent to the holes is significantly greater than that of the weft packing density (δ_{xx}) suggests greater positional correlation between neighboring warp tows than that between neighboring weft tows. This occurs because of the topology of the weave. The warp weavers lie on the relatively straight weft tows allowing for lateral sliding, resisted mainly by compression of neighboring warp tows. The weft tows, on the other hand, are constrained laterally by the interlocking warps under the crossovers but are unconstrained between these points. Lateral motion of a weft tow must be transmitted to its neighboring wefts through the interlocking warp network over length scales longer than a unit cell. Within a
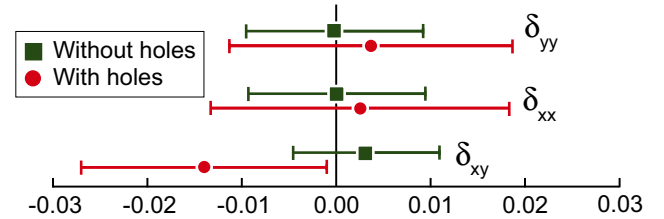

Fig. 4. Summary of averages and standard deviations of derivatives δ_{xx}, δ_{yy}, and δ_{xy}. Also shown for reference are the values for a pristine panel (without holes).[17]

unit cell, each surface weft is not in direct contact with its neighboring surface wefts. Instead, a sizeable gap (~1 mm) exists between adjacent surface wefts, as evident, for example, in Fig. 1(f). Consequently, large lateral displacements would be required in any one weft tow to cause displacement of neighboring surface weft tows.

III. Mechanical Properties

(1) Measurement Methods

Dogbone-shaped tensile specimens were cut from the panel along both the warp and the weft tow directions. Their gauge sections were 25.4 mm long and 12.7 mm wide. The holes (when present) were situated at the center of the gauge section. In preparation for strain mapping by DIC, one face of each specimen was painted white; a black speckle pattern was then created using an airbrush. The regions probed by DIC were 16–17 mm long (centered along the gauge length) and encompassed the full specimen width. The size of the area was selected to maximize strain resolution, especially in the vicinity of the holes. The length of the region of interest represents about twice the unit cell length in the warp direction and about three times the unit cell length in the weft direction. The resulting magnification of the DIC images was 7.1–8.3 μm/pixel. Successful correlation was obtained over the entire area of interest using a subset size of 43–45 pixels (320–360 μm). Two specimens of each type and orientation were tested in uniaxial tension at a nominal strain rate of 10^{-5} s^{-1} at room temperature. All specimens failed within the gauge section.

Global axial strains were computed from displacement measurements made by DIC using linear fits of the axial displacement field $V(x, y)$ for all nodal locations within the correlated region. These were found to be in good agreement with strains measured by axial virtual extensometers as well as the values obtained by averaging strains at all nodal locations. At high applied stress, however, some discrepancies were found with the field-averaged strains, possibly due to the presence of large cracks skewing the average strain upwards. For consistency, the following comparisons in macroscopic mechanical response are made on the basis of the strains obtained from the full displacement field.

The DIC data were also used to characterize local deformation patterns associated with the holes and the fiber architecture. For this purpose, the data were analyzed in three additional complementary forms: (i) as full-field strain maps over the entire correlated area, with strains computed at each nodal location from the measured displacements; (ii) as line scans of axial displacement V with axial position y; and (iii) as strains averaged over areas defined by the specimen width and a length equal to the unit cell dimension in the loading direction, that is, over a length of 5.1 mm in weft-oriented specimens and 7.5 mm in warp-oriented specimens (see insets in Fig. 8). The latter averaging procedure was repeated at 1 mm increments over the specimen length. The area-averaged strains were then plotted against the distance d from the hole center (or the specimen center) to the center of the averaging area (also defined by the insets in Fig. 8).

[‡]$\delta_{xx} = \rho^o_{weft}/\rho_{weft} - 1$, where ρ_{weft} is the packing density of the weft tows and ρ^o_{weft} is the average packing density of the weft tows. Similarly, $\delta_{yy} = \rho^o_{warp}/\rho_{warp} - 1$.
[§]δ_{xy} = half of the cotangent of the angle between warp and weft tows.

Despite considerable smoothing of the preform surface after PIP processing, the underlying fiber tows could be discerned from topographic DIC data. The tow boundaries, obtained from the topographic data and from the optical scans of the preform after CVI, are subsequently superimposed on all strain maps.

(2) Tensile Response of Specimens Without Holes

Under loading in the *weft* direction, the tensile stress–strain curves for test specimens without holes are approximately linear up to about 50 MPa with a Young's modulus $E = 103$–113 GPa [Fig. 5(a)]. Some nonlinearity is obtained in the range 50–100 MPa. Beyond 100 MPa and through to fracture, the response is again approximately linear with a tangent modulus of 43 GPa. By comparison, the modulus calculated on the basis of the volume fraction of weft tows (assumed to be straight) and the reported modulus of T300 fibers ($E_f = 231$ GPa) is $f_{weft}E_f = 49$ GPa: comparable to the measured terminal tangent modulus. The inference is that the matrix has attained a nearly fully damaged state that precludes significant additional load transfer from the fibers to the matrix.[18] In addition, the fiber bundle strength, taken as σ_{ult}/f_{weft} (σ_{ult} being the ultimate strength), is 1.8 GPa. This is in close agreement with the reported bundle strength of T300 fibers (1.8 ± 0.2 GPa).[19]

The stress–strain response of the pristine specimens tested in the *warp* direction [Fig. 5(a)] is more compliant ($E = 65$ GPa), owing mainly to the lower fiber volume fraction in this direction (11% in the warp direction versus 22% in the weft direction). The elastic domain is restricted to stresses ≤25 MPa. A second nearly linear domain is obtained at stresses above about 70 MPa. However, in contrast to the behavior in the weft orientation, the terminal tangent modulus (13 GPa) is only about half of the contribution expected of the warp tows ($f_{warp}E_f = 23$ GPa), again computed assuming that the fibers are initially straight. The difference suggests that the matrix undergoes progressive damage and/or the undulating warp tows undergo some straightening. Furthermore, the inferred fiber bundle strength (σ_{ult}/f_{warp}) is only 1.0 GPa (about half that obtained in the weft direction) and the composite fracture strain is significantly lower than that obtained in the weft direction (0.6% vs 0.8%). The lower values of fracture strain and fiber bundle strength in the warp direction are tentatively attributed to bending loads imparted to the warp tows as these tows attempt to straighten.

Full-field maps of axial strain $\varepsilon_{yy}(x, y)$ at three stress levels are shown in the left columns in Fig. 6. In both orientations, the strains exhibit distinct periodic banded patterns. They are characterized by narrow bands of high apparent strain (well over 1%) and intervening regions with negligible strain.

However, the width of the high-strain regions (~300 μm) is comparable to the subset size used for correlating the DIC data. The inference is that the strains within the bands are not resolved. Based on optical observations of the specimen surfaces and cross sections after testing (presented below), these bands are attributed to the opening of matrix cracks. The displacement discontinuity at each crack appears in the DIC data as a near-linear variation in displacement over a distance comparable to the subset size.[20]

This effect is seen more vividly in line scans of axial displacements $V(y)$, shown in Fig. 7. The scans reveal regions of constant displacement (corresponding to the unstrained regions in Fig. 6) bounded by regions over which the displacement changes from one level to another over a distance comparable to the correlation subset size. Also shown in Fig. 7 are shaded bands indicating the inferred locations of matrix cracks. They are broadly categorized as being either preexisting (determined to be such if the displacement discontinuity was evident from the onset of loading) or as being formed during loading. The former are indicated by the pink-shaded rectangles and the latter by the yellow-shaded rectangles; their width represents the correlation subset size.

This interpretation of the displacement scans was confirmed by micrographs of polished longitudinal cross sections following testing, also shown in Fig. 7. Each displacement jump correlates with a crack in the micrograph at the same location, as indicated on the figures. Furthermore, the locations of the cracks seen in the tested specimens appear to correlate well with the locations of cracks or incipient (filled) cracks evident in cross sections of pristine material, shown in Fig. 1.

The axial variations in the strains averaged over the unit cell lengths at representative stress levels are plotted in Fig. 8. In both orientations, the strains exhibit a periodic (nearly sinusoidal) pattern with a wavelength that is virtually identical to the respective unit cell dimension (i.e., 5.1 mm in the weft direction and 7.5 mm in the warp direction). The amplitude of the variation is about 10% of the average strain in the weft direction and 20%–30% in the warp direction. The implication is that the computed strains are sensitive to the starting and ending points used in defining the local "gauge length" (even though their separation distance is constant). This is likely associated with the small number of cracks (typically about 5–8) over the local gauge length as well as the variations in the opening displacements of the cracks (evident in Fig. 7).

(3) Effects of Holes on Mechanical Behavior

The tensile stress–strain curves for specimens containing holes are plotted in Fig. 5 in two forms: in terms of the remote stress [in Fig. 5(a)] and in terms of the nominal
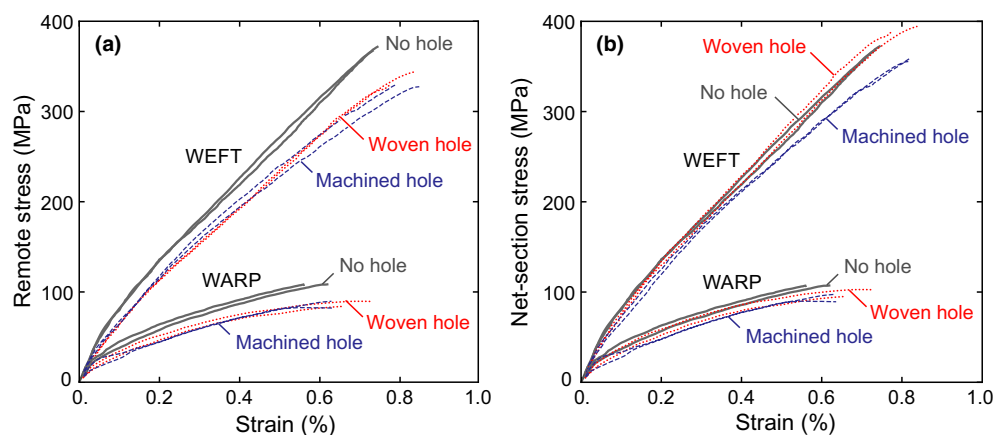

Fig. 5. Tensile stress–strain response of weft- and warp-oriented specimens, couched in terms of (a) remote stress and (b) nominal net-section stress. The curves have been truncated at the load maximum.
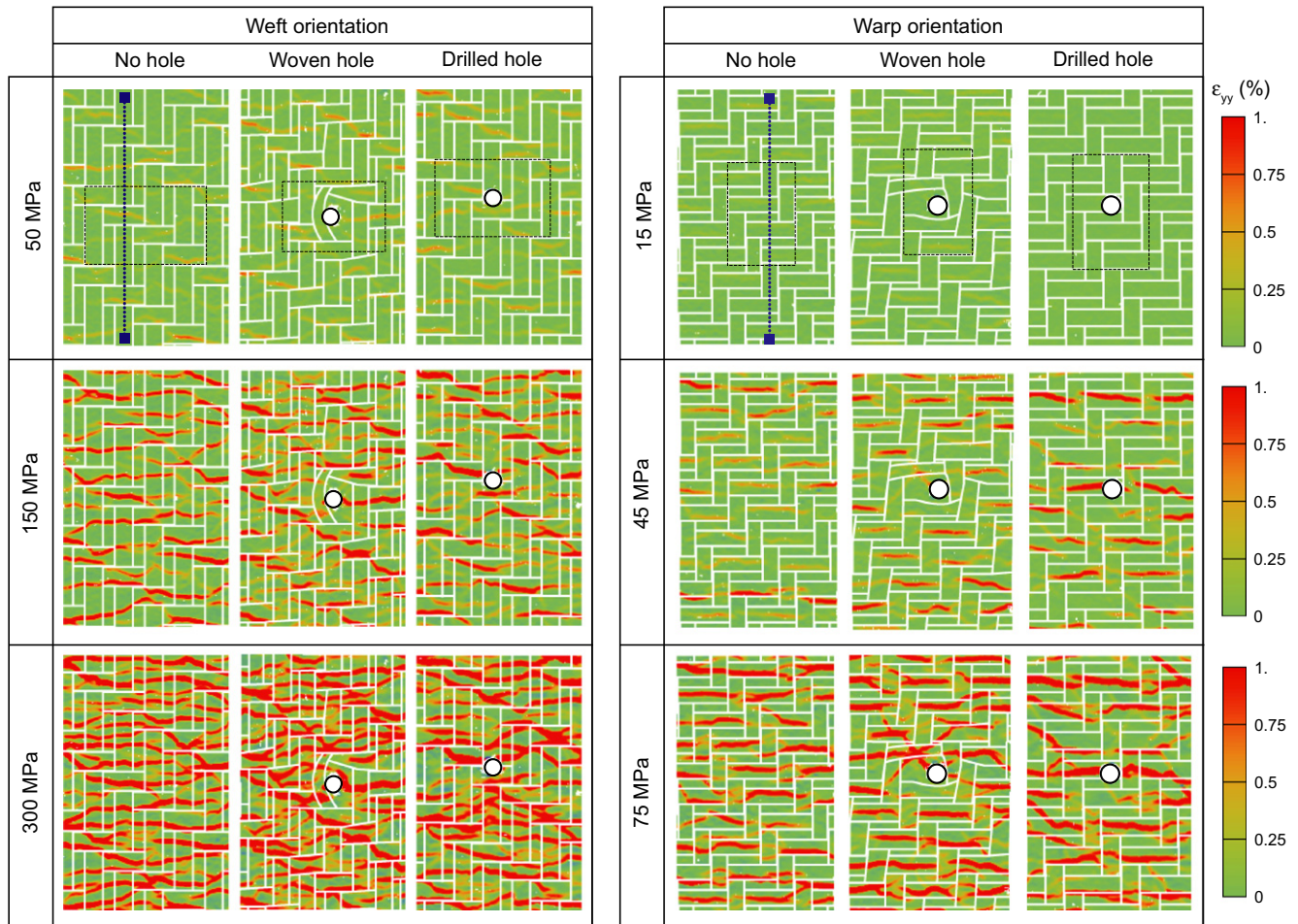
Fig. 6. Full-field axial strains of tensile specimens in weft and warp directions at the stresses indicated. Underlying tow boundaries are overlaid in white. Dashed rectangles represent the unit cell. Dotted line on the top left image of each sequence is the path along which displacement scans were computed and plotted in Fig. 7.

net-section stress [in Fig. 5(b)]. (The latter is defined such that the ratio of the two stresses is $1 - a/w$.) When couched in terms of remote stress, the specimens with holes exhibit slightly higher compliance over the entire strain range and lower UTS relative to those in their respective unnotched specimens. In addition, the failure strains of specimens with holes are slightly higher.

When couched in terms of the nominal net-section stress, the stress–strain curves for specimens with woven holes appear to collapse onto the curves for unnotched specimens in both warp and weft directions. Specimens with machined holes exhibit similar trends (with their stress–strain curves coming into closer agreement with the unnotched results), although they appear to lie consistently slightly below those of the woven holes.

Variations in UTS with hole size are plotted in Fig. 9. The slight strength reductions associated with the holes can be rationalized to first order on the basis of the reduced net-section area. Assuming a critical net-section stress at fracture (without notch sensitivity), the predictions are in broad agreement with the measurements. Examining the results more closely, however, it appears that, in the weft direction, the net-section strength of specimens with woven holes lie slightly above the predictions, by about 5%; in contrast, those with machined holes exhibit strengths that are about 5% lower than the predictions. For tests in the warp direction, specimens with both woven and machined holes consistently lie slightly below the prediction, by about 5%.

Full-field axial strain maps for these specimens are shown in Fig. 6, at remote stress levels that correspond to those of

the specimens without holes. Here, again, the strain fields are characterized by banded patterns reflecting the opening of matrix cracks. Within the resolution of the present measurements, the patterns appear to evolve independently of the holes. That is, there does not appear to be an increased propensity for cracking in regions of high stress concentration adjacent to the holes. If the holes behaved as stress concentrators, the strains would be highest along the transverse plane containing the hole and would diminish rapidly with distance from the hole to the far field value: the latter being comparable to the strain obtained in the pristine (unnotched) specimen at the same applied stress.

An additional attempt at quantifying the preceding effects was made by examining the variations in axial strain averaged over one unit cell length with axial distance from the hole center. This exercise is based on the expectation (previously noted) that the strains should be elevated in the vicinity of the holes and should diminish in regions remote from the holes. The results are plotted in Fig. 8. As with the unnotched specimens, the strain distributions of specimens with holes exhibit periodic patterns with wavelengths similar to the pertinent unit cell dimension. The patterns also reveal effects of the holes. Specifically, the strain distributions appear to be a convolution of the periodic variations associated with the weave geometry and the more-local effects of the holes near the specimen centers. Although the strains for the unit cells centered on the holes (at $d = 0$ in Fig. 8) are elevated somewhat in most specimens, the longer range effects of the holes appear to be masked by the effects of the weave. Furthermore, as the data probe regions that are only a relatively short distance from the hole (selected to
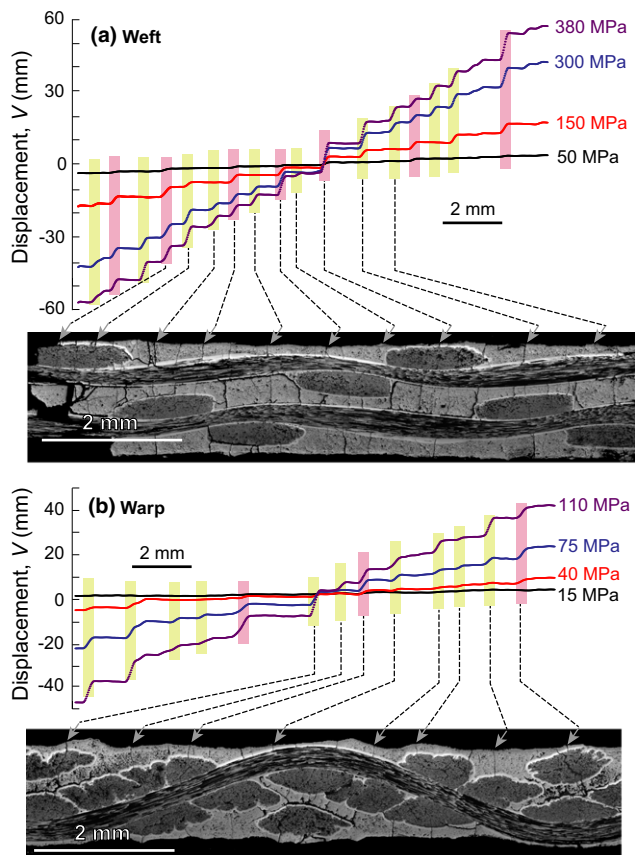
Fig. 7. Line scans of axial displacement, *v*, highlighting the development of cracks at representative stress levels. Also shown are micrographs of optical cross sections of the fractured specimens and the correlations between the cracks and the displacement jumps. (a) Weft direction; (b) warp direction.

maximize strain resolution), the average composite strains remote from the hole could not be ascertained.

Further insights into the operative damage mechanisms were gleaned from maps of the full-field *transverse* ε_{xx} *and shear strains* ε_{xy} at high stresses, shown in Fig. 10. Several features are noteworthy. First, when loaded in the warp direction, the composite exhibits vertical bands of compressive transverse strains along the center of each warp tow (blue bands indicating strain of ~0.5%), likely produced by closing of preexisting matrix cracks aligned with the loading directions [see, e.g., Figs. 1(c)–(e)]. Conversely, bands of transverse *tensile* strains are obtained in the weft tows, indicative of crack opening. The latter effects appear somewhat more pronounced in the specimens with holes, especially the holes that had been woven. Similar effects are obtained in the weft-oriented specimens. In this case, bands of compressive strain are obtained at the center of some of the weft tows and bands of tensile strain in some of the warp tows, although their prevalence is lower than those in the warp specimens. The effects become more pronounced in the presence of holes, especially in regions near the holes. Here, again, given the resolution of measurements, the rather short specimen length and the large unit cell size, the local effects attributable to the holes cannot be readily ascertained.

Similar trends are obtained in the shear strain distributions. They consist of two families of inclined bands of positive and negative shear. Their magnitude increases in the presence of holes, especially in regions close to the hole. Of particular note is the response of the weft coupon with a machined hole, which exhibits a pattern of inclined shear bands extending vertically above and below the hole. This is suggestive of shear transfer to the cut tows passing through the hole.
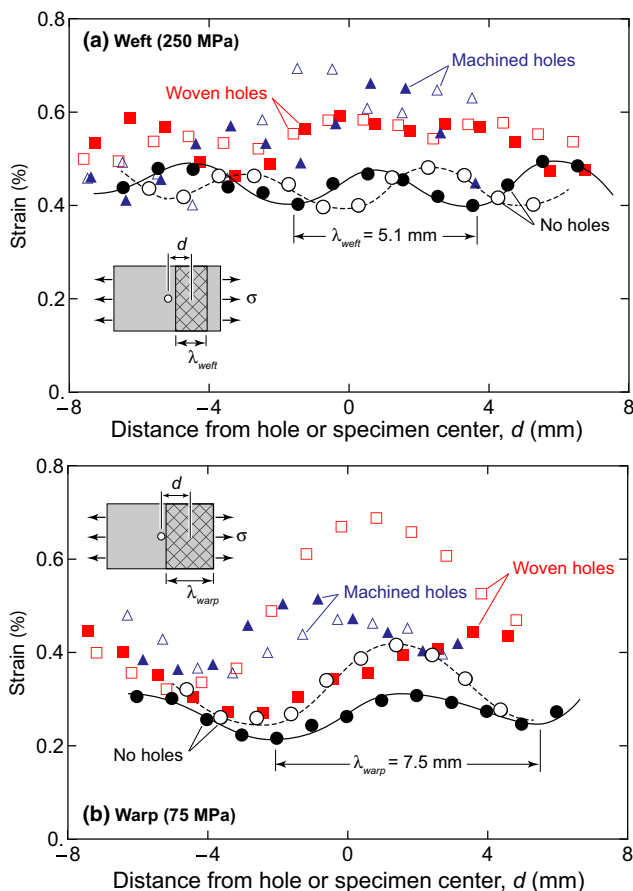

Fig. 8. Average axial strain as a function of distance from the hole center for (a) weft-oriented specimens at a stress of 250 MPa, and (b) warp-oriented specimens at a stress of 75 MPa. Open and closed symbols correspond to individual specimens within a group. For the specimens without holes, the distance is measured from the specimen center. Dashed and solid curves represent approximate fits to the datasets for specimens without holes. Insets show the areas over which the strains were computed and the manner in which the distance *d* was ascertained.
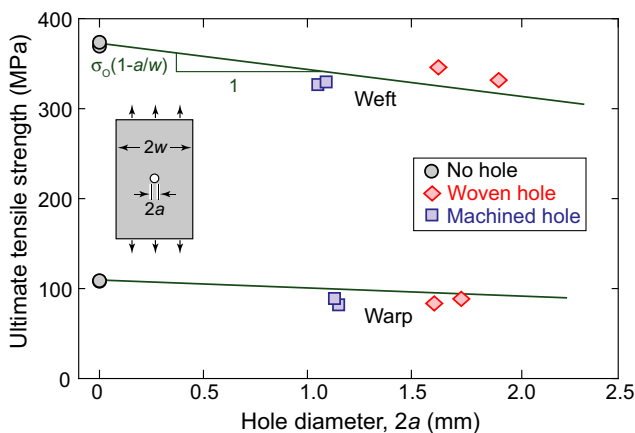

Fig. 9. Variation in ultimate tensile strength (based on remote stress) with hole diameter in warp and weft orientations. Solid lines represent predictions based on a critical net-section stress at fracture, calibrated using the unnotched tensile strength, σ_O (at $a = 0$).

IV. Discussion and Conclusions

A study has been conducted to probe the tensile properties of a woven anisotropic C/SiC composite. In both warp and weft orientations, the surface (matrix) strains are accommodated largely by the opening of preexisting matrix cracks, initially either open or partially filled during the PIP process. In
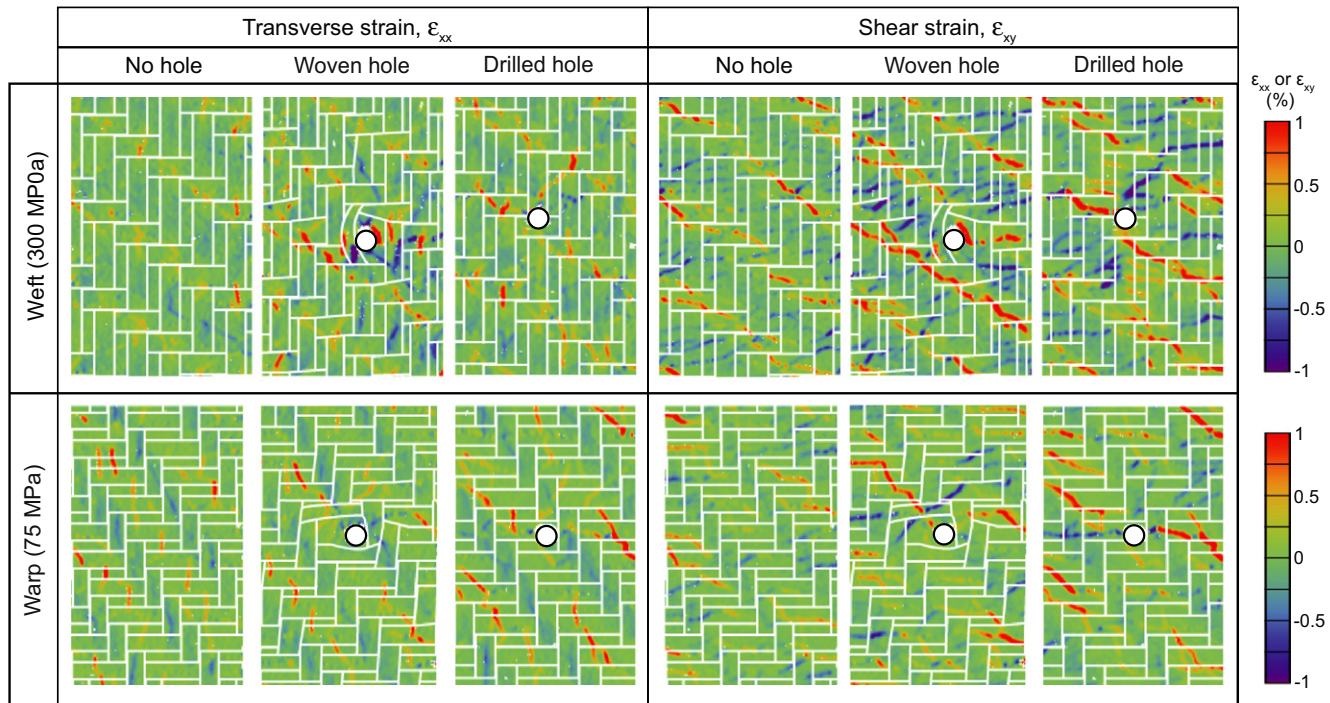
Fig. 10. Maps of transverse and shear strain fields near the ultimate tensile strength of specimens in warp and weft directions.

the *weft* orientation, the load supported by the matrix appears to reach a near-constant value at a low applied stress, as manifest in a near-constant tangent modulus. The slight reduction in tangent modulus in the late stages of the tensile tests can be attributed to the formation of some additional (new) cracks, as inferred from the displacement line scans. With the weft tows being rather straight, the composite tensile strength in this orientation is essentially the same as the reported bundle strength for the fibers alone.

Although similar patterns of crack evolution are obtained in the *warp* orientation, the tangent modulus is significantly lower than the contribution that would be expected from straight aligned fibers (by almost a factor of 2), suggesting an important role of tow straightening. In addition, the initial tow waviness and attendant straightening leads to bending stresses that, when superimposed on the axial tension, result in reductions in UTS and failure strain relative to those expected from straight axial tows.

When averaged over lengths equal to the unit cell dimensions, the strains exhibit periodic variations along the loading direction with a wavelength that corresponds closely to the pertinent unit cell dimension. Evidently the representative volume elements needed to capture the macroscopic material behavior are greater than the unit cell dimensions. The effect is attributable to the rather small number of cracks within each unit cell that control the degree of inelastic strain.

Holes can be introduced into the fiber preform prior to matrix infiltration, thereby minimizing the extent of fiber damage (relative to that obtained when the holes are machined after processing). The holes produced in this manner cause negligible distortion of the surrounding weft tows and only small changes in warp tow packing density. In light of the resolution of the measurements and the observation that the apparent disturbances in warp packing persist only over distances of about one unit cell size, the nature and magnitude of the disturbance cannot be characterized completely using the methods employed here. However, optical examinations of the weave in the vicinity of the holes confirm that the effects are indeed very localized.

The UTS of the composite exhibits only a weak sensitivity to the presence of small holes (1–2 mm in diameter), regardless of the manner in which the holes are introduced. Nevertheless, woven holes appear to be less detrimental to strength

in the weft direction than those that had been drilled (by about 10%). The effects can be attributed to the fact that the tows in specimens with woven holes are largely displaced laterally (and perhaps in the through-thickness direction) and thus continue to contribute to the load-bearing capacity. Such effects appear to be small for loading in the warp direction.

When averaged over a unit cell length, the axial strains in specimens with holes exhibit convoluted effects of the weave geometry and the concentration associated with the hole. The present experiments are insufficient to properly parse these contributions to the strain distributions. Nevertheless, it is interesting to note that when the tensile response is couched in terms of net-section stress and average strain, the results for the woven holes collapse onto those for the unnotched specimens, suggesting a rather long-range effect of the holes (at least up to distances of about 1–1.5 unit cells away from the holes). The strains obtained in specimens with drilled holes are consistently higher, a consequence of the absence of fibers in the region of the holes.

Finally, it should be noted that surface strain measurements provide only a partial glimpse into the complex three-dimensional damage processes that operate in woven CMCs. These can only be viewed effectively via synchrotron X-ray tomography,[21] albeit within much smaller test volumes. Combining 2D and 3D imaging techniques with computational approaches based on augmented finite element methods[22] and/or particle-based methods will be required to develop a more comprehensive understanding.

References

[1]J. C. McNulty, F. W. Zok, G. M. Genin, and A. G. Evans, "Notch-Sensitivity of Fiber-Reinforced Ceramic-Matrix Composites: Effects of Inelastic Straining and Volume-Dependent Strength," *J. Am. Ceram. Soc.*, **82** [5] 1217–28 (1999).

[2]C. G. Levi, J. Y. Yang, B. J. Dalgleish, F. W. Zok, and A. G. Evans, "Processing and Performance of an All-Oxide Ceramic Composite," *J. Am. Ceram. Soc.*, **81** [8] 2077–86 (1998).

[3]F. E. Heredia, S. M. Spearing, T. J. Mackin, M. Y. He, A. G. Evans, P. Mosher, and P. Brø ndsted, "Notch Effects in Carbon Matrix Composites," *J. Am. Ceram. Soc.*, **77** [11] 2817–27 (1994).

[4]A. Haque, L. Ahmed, and A. Ramasetty, "Stress Concentrations and Notch Sensitivity in Woven Ceramic Matrix Composites Containing a Circular Hole-an Experimental, Analytical, and Finite Element Study," *J. Am. Ceram. Soc.*, **88** [8] 2195–201 (2005).

[5]C. Cady, T. Mackin, and A. Evans, "Silicon Carbide/Calcium Aluminosilicate: A Notch-Insensitive Ceramic-Matrix Composite," *J. Am. Ceram. Soc.*, **78** [1] 77–82 (1995).

[6]W. Keith and K. Kedward, "Notched Strength of Ceramic-Matrix Composites," *Compos. Sci. Technol.*, **57** [6] 631–5 (1997).

[7]Y. Kogo, H. Hatta, H. Kawada, and T. Machida, "Effect of Stress Concentration on Tensile Fracture Behavior of Carbon-Carbon Composites," *J. Compos. Mater.*, **32** [13] 1273–94 (1998).

[8]J. C. McNulty, M. Y. He, and F. W. Zok, "Notch Sensitivity of Fatigue Life in a Sylramic TM/SiC Composite at Elevated Temperature," *Compos. Sci. Technol.*, **61** [9] 1331–8 (2001).

[9]M. B. Ruggles-Wrenn and G. Kurtz, "Notch Sensitivity of Fatigue Behavior of a Hi-Nicalon™/SiC-B4C Composite at 1200°C in Air and in Steam," *Appl. Compos. Mater.*, **20** [5] 891–905 (2013).

[10]H. J. Lin and Y. J. Lee, "Strength of Composite Laminates with Continuous Fiber Around a Circular Hole," *Compos. Struct.*, **21** [3] 155–62 (1992).

[11]A. Nakai, T. Ohki, N. Takeda, and H. Hamada, "Mechanical Properties and Micro-Fracture Behaviors of Flat Braided Composites with a Circular Hole," *Compos. Struct.*, **52** [3–4] 315–22 (2001).

[12]D. B. Marshall and B. N. Cox, "Integral Textile Ceramic Structures," *Annu. Rev. Mater. Res.*, **38**, 425–43 (2008).

[13]B. N. Cox, H. A. Bale, M. Begley, M. Blacklock, B.-C. Do, T. Fast, M. Naderi, M. Novak, V. P. Rajan, R. G. Rinaldi, R. O. Ritchie, M. N. Rossol, J. H. Shaw, O. Sudre, Q. Yang, F. W. Zok, and D. B. Marshall, "Stochastic Virtual Tests for High-Temperature Ceramic Matrix Composites," *Annu. Rev. Mater. Res.*, **44**, 479–529 (2014).

[14]H. Bale, M. Blacklock, M. Begley, R. O. Ritchie, D. B. Marshall, and B. N. Cox, "Characterizing Three-Dimensional Textile Ceramic Composites Using Synchrotron x-ray Micro-Computed-Tomography," *J. Am. Ceram. Soc.*, **95** [1] 392–402 (2012).

[15]M. Blacklock, H. Bale, M. Begley, and B. N. Cox, "Generating Virtual Textile Composite Specimens Using Statistical Data from Micro-Computed Tomography: 1D Tow Representations for the Binary Model," *J. Mech. Phys. Solids*, **60** [3] 451–70 (2012).

[16]R. G. Rinaldi, M. Blacklock, H. Bale, M. R. Begley, and B. N. Cox, "Generating Virtual Textile Composite Specimens Using Statistical Data from Micro-Computed Tomography: 3D Tow Representations," *J. Mech. Phys. Solids*, **60** [8] 1561–81 (2012).

[17]M. N. Rossol, T. Fast, D. B. Marshall, B. N. Cox, and F. W. Zok, "Characterizing In-Plane Geometrical Variability in Textile Ceramic Composites," *J. Am. Ceram. Soc.*, (in press). doi: 10.1111/jace.13275.

[18]B. Budiansky, J. W. Hutchinson, and A. G. Evans, "Matrix Fracture in Fiber-Reinforced Ceramics," *J. Mech. Phys. Solids*, **34** [2] 167–89 (1986).

[19]M. R'Mili, T. Bouchaour, and P. Merle, "Estimation of Weibull Parameters from Loose-Bundle Tests," *Compos. Sci. Technol.*, **3538** [56] 831–4 (1996).

[20]V. P. Rajan, M. N. Rossol, and F. W. Zok, "Optimization of Digital Image Correlation for High-Resolution Strain Mapping of Ceramic Composites," *Exp. Mech.*, **52** [9] 1407–21 (2012).

[21]H. A. Bale, A. Haboub, A. A. MacDowell, J. R. Nasiatka, D. Y. Parkinson, B. N. Cox, D. B. Marshall, and R. O. Ritchie, "Real-Time Quantitative Imaging of Failure Events in Materials Under Load at Temperatures Above 1600°C," *Nat. Mater.*, **12** [1] 40–6 (2013).

[22]D. Ling, Q. Yang, and B. Cox, "An Augmented Finite Element Method for Modeling Arbitrary Discontinuities in Composite Materials," *Int. J. Fract.*, **156** [1] 53–73 (2009). □